

WRDC-TR-89-3034

LOW DENSITY FLOW EFFECTS FOR HYPERVELOCITY VEHICLES

Roop N. Gupta

Vigyan Research Associates, Inc.
30 Research Drive
Hampton, VA 23666-1325

March 1989

Final Report for Period August 1986 - July 1987



Approved for Public Release; Distribution Unlimited

FLIGHT DYNAMICS LABORATORY
WRIGHT RESEARCH AND DEVELOPMENT CENTER
AIR FORCE SYSTEMS COMMAND
WRIGHT-PATTERSON AIR FORCE BASE, OHIO 45433-6553

89 3 29 005

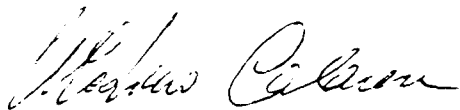
AD-A206 218

NOTICE

When Government drawings, specifications, or other data are used for any purpose other than in connection with a definitely Government-related procurement, the United States Government incurs no responsibility or any obligation whatsoever. The fact that the government may have formulated or in any way supplied the said drawings, specifications, or other data, is not to be regarded by implication, or otherwise in any manner construed, as licensing the holder, or any other person or corporation; or as conveying any rights or permission to manufacture, use, or sell any patented invention that may in any way be related thereto.

This report is releasable to the National Technical Information Service (NTIS). At NTIS, it will be available to the general public, including foreign nations.

This technical report has been reviewed and is approved for publication.



WLADIMIRO CALARESE
Aerospace Engineer
WRDC/FIMG

FOR THE COMMANDER



VALENTINE DAHLEM, Chief
WRDC/FIMG



ALFRED C. DRAPER
Acting Chief, Aeromechanics Division
Flight Dynamics Laboratory

If your address has changed, if you wish to be removed from our mailing list, or if the addressee is no longer employed by your organization please notify WRDC/FIMG, WPAFB, OH 45433-6553 to help us maintain a current mailing list.

Copies of this report should not be returned unless return is required by security considerations, contractual obligations, or notice on a specific document.

UNCLASSIFIED

SECURITY CLASSIFICATION OF THIS PAGE

REPORT DOCUMENTATION PAGE

Form Approved
OMB No. 0704-0188

| | | | | | |
|---|-------|---|--|---|---------------------------------|
| 1a. REPORT SECURITY CLASSIFICATION UNCLASSIFIED | | | 1b. RESTRICTIVE MARKINGS | | |
| 2a. SECURITY CLASSIFICATION AUTHORITY | | | 3. DISTRIBUTION / AVAILABILITY OF REPORT Approved for Public Release; Distribution unlimited | | |
| 2b. DECLASSIFICATION / DOWNGRADING SCHEDULE | | | | | |
| 4. PERFORMING ORGANIZATION REPORT NUMBER(S) | | | 5. MONITORING ORGANIZATION REPORT NUMBER(S) WRDC-TR-89-3034 | | |
| 6a. NAME OF PERFORMING ORGANIZATION Vigyan Research Associates, Inc | | 6b. OFFICE SYMBOL (If applicable) | 7a. NAME OF MONITORING ORGANIZATION Flight Dynamics Laboratory (WRDC/FIMG) Wright Research and Development Center | | |
| 6c. ADDRESS (City, State, and ZIP Code) 30 Research Drive Hampton VA 23666-1325 | | | 7b. ADDRESS (City, State, and ZIP Code) Wright-Patterson AFB OH 45433-6553 | | |
| 8a. NAME OF FUNDING / SPONSORING ORGANIZATION | | 8b. OFFICE SYMBOL (If applicable) | 9. PROCUREMENT INSTRUMENT IDENTIFICATION NUMBER F33615-86-C-3009 | | |
| 8c. ADDRESS (City, State, and ZIP Code) | | | 10. SOURCE OF FUNDING NUMBERS | | |
| | | | PROGRAM ELEMENT NO. 65502F | PROJECT NO. 3005 | TASK NO. 30 |
| 11. TITLE (Include Security Classification) Low Density Flow Effects for Hypervelocity Vehicles (U) | | | | | |
| 12. PERSONAL AUTHOR(S) Roop N. Gupta | | | | | |
| 13a. TYPE OF REPORT Final | | 13b. TIME COVERED FROM 8/1/86 TO 7/10/87 | | 14. DATE OF REPORT (Year, Month, Day) 1989 March | |
| 15. PAGE COUNT 41 | | | | | |
| 16. SUPPLEMENTARY NOTATION | | | | | |
| 17. COSATI CODES | | | 18. SUBJECT TERMS (Continue on reverse if necessary and identify by block number) Hypersonic Viscous Flow Low Density Flow | | |
| FIELD | GROUP | SUB-GROUP | | | |
| 0101 | 2004 | 2013 | | | |
| | | | | | |
| 19. ABSTRACT (Continue on reverse if necessary and identify by block number) This work presents results for the surface pressure, drag, heat transfer and skin-friction coefficients for hyperboloids and sphere-cone shaped slender and wide-angle bodies under varying degrees of low-density flow conditions. Recently obtained surface-slip and the corrected shock-slip conditions are employed to account for the low-density effects. The flow cases analyzed include highly cooled and very long slender bodies in high Mach number flows. The present method (limited to the analysis of a perfect-gas here) is found to predict various flow field quantities quite accurately when compared with the experimental data. | | | | | |
| 20. DISTRIBUTION / AVAILABILITY OF ABSTRACT <input type="checkbox"/> UNCLASSIFIED/UNLIMITED <input type="checkbox"/> SAME AS RPT. <input checked="" type="checkbox"/> DTIC USERS | | | 21. ABSTRACT SECURITY CLASSIFICATION UNCLASSIFIED | | |
| 22a. NAME OF RESPONSIBLE INDIVIDUAL WLADIMIRO CALARESE | | | 22b. TELEPHONE (Include Area Code) (513) 255-2052 | | 22c. OFFICE SYMBOL WRDC/FIMG |

Nomenclature

| | |
|--------------------|---|
| C_D | drag coefficient based on the local cross-section area, $2 \text{ Drag}/(\rho_\infty^* U_\infty^{*2} A^*)$ |
| C_f | skin friction coefficient, $2 \tau_w^*/(\rho_\infty^* U_\infty^{*2})$ |
| C_p^* | specific heat at constant pressure |
| g | stretching function |
| H | total enthalpy, H^*/U_∞^{*2} |
| H^* | $= h^* + u^{*2}/2$ |
| h | static enthalpy, h^*/U_∞^{*2} |
| K | thermal conductivity, $K^*/\mu_{\text{ref}}^* C_{p,\infty}^*$ |
| K^* | thermal conductivity |
| M_∞ | freestream Mach number |
| n | coordinate measured normal to the body, n^*/R_N^* |
| Pr | Prandtl number, $C_p^* \mu^*/K^*$ |
| p | pressure, $p^*/(\rho_\infty^* U_\infty^{*2})$ |
| q | heat transfer, $q^*/(\rho_\infty^* U_\infty^{*3})$ |
| R_N^* | body nose radius |
| r | radius measured from axis of symmetry to a point on the body surface, r^*/R_N^* |
| St | Stanton number, $St = -q/(H_\infty - H_w)$ |
| s | coordinate measured along the body surface, s^*/R_N^* |
| T | temperature, T^*/T_{ref}^* |
| T_{ref}^* | $U_\infty^{*2}/C_{p,\infty}^*$ |
| U_∞^* | freestream velocity |
| u | velocity component tangent to body surface, u^*/U_∞^* |
| v | velocity component normal to body surface, v^*/U_∞^* |

α shock angle defined in Fig. 1
 $\bar{\alpha}$ mesh refinement parameter
 $\alpha_1, \alpha_2, \alpha_3, \alpha_4$ } coefficients in Eq. (1)
 β angle defined in Fig. 1
 $\bar{\beta}$ mesh refinement parameter
 γ ratio of specific heats
 ϵ Reynolds number parameter, $\epsilon = [\mu_{\text{ref}}^* / \rho_{\infty}^* U_{\infty}^* R_N^*]^{1/2}$
 η transformed $\bar{\eta}$ coordinate, $g(\bar{\eta})$
 $\bar{\eta}$ transformed n coordinate, n/n_{sh}
 θ body angle defined in Fig. 1
 $\bar{\theta}$ accommodation coefficient
 κ body curvature, $\kappa^* R_N^*$
 μ viscosity, $\mu^* / \mu_{\text{ref}}^*$
 μ_{ref}^* reference viscosity, $\mu^*(T_{\text{ref}}^*)$
 ξ coordinated measured along the body surface, $\xi = s$
 ρ density, ρ^* / ρ_{∞}^*
 τ shear stress, $\tau^* / (\rho_{\infty}^* U_{\infty}^{*2})$

Subscripts

s value at edge of Knudsen layer
 sh shock value
 w wall value
 ∞ freestream value

Superscripts

j zero for plane flow and one for axisymmetric flow
 \sim shock oriented velocity components
 $'$ total differential
 $*$ dimensional quantity

INTRODUCTION AND RELEVANCE OF THE PROBLEM

The recently increased interest in space for civilian and defense purposes has resulted in new concepts for the hypersonic vehicles. The Aeroassisted and Aeromaneuvering Orbital Transfer Vehicles (Refs. 1-2) (AOTVs and AMOTVs), the Transatmospheric Vehicles (TAVs) and/or Orbit-On-Demand (OOD) vehicles (Ref. 3), the Hypersonic Cruise and Manuever Airplanes (HCMA) (Ref. 4), and the present (Ref. 5) and next generation space shuttles, are a few of the examples of these vehicles which have created a resurgence of interest in hypersonic aerothermodynamics.

Since most of the future hypersonic vehicles will be operating in the upper atmosphere, the 'low density effects' will play a major role in establishing the lift, drag, moments, and aerodynamic heating of a hypersonic vehicle. In addition, the new vehicular concepts will require more accurate knowledge of hypersonic aerothermodynamics under the low density conditions. The so-called 'shock and surface slip effects,' multicomponent nonequilibrium gas chemistry, proper modeling of gas-surface interactions, reaction-rate coefficients for high temperature air as well as a correct description of thermodynamic and transport properties would be the pacing research activities for an accurate prediction of the aerothermal environment of the new generation of hypersonic vehicles.

The problems of hypersonic aerodynamics without the low density effects have been analyzed in detail (Refs. 6-17) both for perfect gas as well as for air with real gas effects. Not much attention seems to have been given to the problems encountered with low-density aerothermodynamics. Reference 18 analyzed the flow past a flat plate at low densities with body slip only. Davis (Ref. 19) included body and shock-slip in the viscous shock-layer

analysis of perfect-gas flow around a hyperboloid. The low-density shock thickening effects with the integration of full Navier-Stokes equations in the stagnation region were recently obtained in Ref. 20.

The surface slip conditions obtained by Davis (Ref. 19) contained some errors as explained in Ref. 21. The shock-slip boundary condition of Ref. 19 also did not account for the derivatives of the shock quantities in the shock-oriented coordinate system. This introduces significant errors in analyzing flows past slender bodies as compared to the wide-angle bodies. Tree, et al. (Ref. 22), analyzed the hypersonic ionizing viscous shock-layer flow past axially symmetric bodies at low densities. Their analysis was for an equilibrium catalytic wall and contained the errors of Ref. 19 in the specification of body- and shock-slip boundary conditions. Swaminathan, et al. (Ref. 23) and Song, et al. (Ref. 24) recently included the surface- and shock-slip effects for the three-dimensional flows. Their shock-slip formulation contained the error mentioned earlier, whereas their surface-slip model was taken from Ref. 25, which also contained errors as explained in Ref. 21. Further, even without the shock- and surface-slip boundary conditions, the viscous shock-layer (VSL) three-dimensional code of Refs. 23 and 24 gives flowfield quantities (such as boundary layer thickness, flowfield profiles of velocity, temperature, etc.), which are physically not very appealing (Ref. 26). The surface heat transfer and skin-friction coefficient predicted by the code developed by Clark Lewis and his associates (Refs. 23 and 24) is impacted considerably by these poor flowfield quantities for a turbulent flow as shown in Ref. 26. The inaccurate flowfield profiles have also resulted in poor comparison of predicted surface heat transfer with the shuttle flight data (Ref. 27). One of the major drawback with Lewis' code is that it smooths the

shock-stand-off distance after each global flowfield solution, resulting in poor conservation of mass and momentum in the flowfield. Instead, in the code developed here, the streamwise derivatives of the shock stand-off distance are smoothed. This results in superior conservation of mass and momentum in the flowfield.

An additional premium is placed on the theoretical analysis by the fact the most of the ground-based experimental facilities fail to simulate the low-density highly energetic flowfields. In particular, the interaction between a high enthalpy gas flow and a relatively cold surface for the low-density hypersonic re-entry conditions is poorly simulated (at best) with the existing experimental facilities. These limitations in the simulation by ground-based facilities resulted in the design of the Galileo heat shield (Refs. 14-17, 28) completely by means of detailed flowfield calculations. This is considered a 'first' in modern hypersonics where no experimental data in the final design of heat shield were used since they were not available. Thus, there is a need to develop an accurate viscous shock-layer code which can give physically appealing results over a wide range of flow conditions.

The viscous shock-layer (VSL) analysis (Ref. 11) is one of the most extensively used continuum computational techniques for analyzing the flowfields past two-dimensional and axisymmetric bodies of revolution at hypersonic velocities. The method of reference 11 has been used both for perfect gas as well as for air with finite-rate chemistry to allow for the real gas effects. Most of the results obtained so far with the VSL method of Ref. 11 do not allow for the low-density effects and the shock is treated as a thin discontinuity. The main advantages of the VSL method are that even with multicomponent gas chemistry, it can give results around the complete body in

a very small computational time and also the computer storage requirements are relatively small. The major deficiencies of the VSL code of Ref. 11 are that it does not account for the low-density effects as well as it fails to converge for slender bodies (such as sphere cones with body half-angles of less than 25°).

Reference 20 employs the complete Navier-Stokes equations where no assumption is made about the shock thickness and the shock is captured as part of the solution. The main disadvantage with this approach is large storage requirement because the numerical integration is carried out to the free-stream. The computational times will also vary large if solutions are desired around a complete body. These solutions, however, can serve the basis for changes and/or improvements required in the VSL technique under low density conditions.

In comparison to the noncontinuum methods like the Direct Simulation Monte Carlo (Ref. 29) (DSMC), etc., the continuum methods (such as VSL and Navier-Stokes) are fast and give practical results in a fraction of the computational time. The recent work (Refs. 5, 20, 21) shows the accuracy of continuum prediction techniques if proper accounting is made of the low-density effects.

As mentioned earlier, the experimental data for the low-density high energy flows are almost non-existent in the literature. For low energy flows and for shapes with spherically-blunted nose-tips (such as hyperboloids and sphere cones), Refs. 30 and 31 have provided good data. Little's data (Ref. 30) are limited to the measurements of pressure, drag, and skin friction, whereas Boylon's data (Ref. 31) are for the surface heat transfer. These measurements were made during the nineteen-sixties and early nineteen-

seventies. Thus, there is a considerable need to have the experimental, in particular, surface heat transfer data under the low density flow conditions. With the superior data acquisition and reduction techniques available now, it should be possible to obtain the new data with fairly high degree of accuracy.

PRESENT WORK

With the deficiencies and inadequacies of the continuum techniques (outlined in the introduction) in mind, a viscous shock-layer (VSL) code has been developed for the low density flight conditions for wide-angle as well as long slender bodies. Under the low Reynolds number (or low-density) flow conditions, the viscous effects influence almost the entire shock-layer and the shock itself is considerably thick as compared to the high Reynolds number (or high-density) case. This requires the use of more comprehensive set of governing equations as compared to the classical boundary-layer equations. The complete Navier-Stokes equations are considered (Ref. 20) appropriate for the low Reynolds number applications. But computer storage and computational time-wise they are very expensive to solve for flows around the long bodies. The viscous shock-layer (VSL) equations (Refs. 11, 16, 19) represent an intermediate level of approximation between the boundary-layer and Navier-Stokes equations. In obtaining the viscous shock-layer equations from the Navier-Stokes equations, terms are kept up to second-order in the inverse square root of the Reynolds number from both a viscous and inviscid viewpoint. This results in simplified governing equations, which are uniformly valid to moderately low Reynolds numbers. To the order of approximation involved in obtaining the VSL equations, the body surface conditions are given by slip and

temperature jump conditions (Ref. 21) while a set of shock-slip conditions* are used to determine conditions behind the shock.

ANALYSIS

Flow Governing Equations

The conservation equations employed in the present analysis are the steady perfect-gas viscous shock-layer equations (Refs. 11 and 19) for an axisymmetric or two-dimensional body at zero angle of attack (Fig. 1). These equations in the orthogonal, body-oriented transformed coordinates and nondimensional form are provided here. The second-order partial differential equations are written in the following form:

$$\begin{aligned} \frac{\partial^2 W}{\partial \bar{\eta}^2} + \frac{(\partial^2 g / \partial \bar{\eta}^2) + \alpha_1 (\partial g / \partial \bar{\eta})}{(\partial g / \partial \bar{\eta})^2} \frac{\partial W}{\partial \bar{\eta}} + \frac{\alpha_2}{(\partial g / \partial \bar{\eta})^2} W \\ + \frac{\alpha_3}{(\partial g / \partial \bar{\eta})^2} + \frac{\alpha_4}{(\partial g / \partial \bar{\eta})^2} \frac{\partial W}{\partial \xi} = 0. \end{aligned} \quad (1)$$

The quantity W represents u in the s -momentum equation and H in the enthalpy energy equation. The coefficients α_1 to α_4 are written as follows:

s -momentum, $W = u$:

$$\begin{aligned} \alpha_1 = \frac{1}{\mu} \frac{\partial \mu}{\partial \bar{\eta}} \frac{\partial g}{\partial \bar{\eta}} + \frac{n_{sh} \kappa}{1 + \bar{\eta} n_{sh} \kappa} + \frac{j n_{sh} \cos \theta}{r + \bar{\eta} n_{sh} \cos \theta} \\ + \frac{n'_{sh} n_{sh} \bar{\eta} \rho u}{\epsilon^2 (1 + \bar{\eta} n_{sh} \kappa) \mu} - \frac{n_{sh} \rho v}{\epsilon^2 \mu} \end{aligned} \quad (2a)$$

*These are similar to those of Ref. 19 except for the corrections to tangential velocity and temperature slip expressions.

$$\alpha_2 = - \frac{n_{sh}^2 \kappa}{(1 + \bar{n} n_{sh} \kappa)} \frac{\partial \mu}{\partial \eta} \frac{\partial g}{\partial \bar{n}} - \frac{n_{sh}^2 \kappa}{(1 + \bar{n} n_{sh} \kappa)} \left[\frac{\kappa}{1 + \bar{n} n_{sh} \kappa} + \frac{j \cos \theta}{r + \bar{n} n_{sh} \cos \theta} \right] - \frac{n_{sh}^2 \kappa \rho v}{\epsilon^2 (1 + \bar{n} n_{sh} \kappa) \mu} \quad (2b)$$

$$\alpha_3 = - \frac{n_{sh}^2}{\epsilon^2 (1 + \bar{n} n_{sh} \kappa) \mu} \left\{ \frac{\partial p}{\partial \xi} - \frac{n'_{sh} \bar{n}}{n_{sh}} \frac{\partial p}{\partial \eta} \frac{\partial g}{\partial \bar{n}} \right\} \quad (2c)$$

$$\alpha_4 = - \frac{n_{sh}^2 \rho u}{\epsilon^2 (1 + \bar{n} n_{sh} \kappa) \mu} \quad (2d)$$

Energy, $W = H$:

$$\alpha_1 = \frac{1}{(\mu/Pr)} \frac{\partial(\mu/Pr)}{\partial \eta} \frac{\partial g}{\partial \bar{n}} + \frac{\kappa n_{sh}}{1 + \bar{n} n_{sh} \kappa} + \frac{j n_{sh} \cos \theta}{r + \bar{n} n_{sh} \cos \theta} + \frac{n'_{sh} n_{sh} \bar{n} \rho u}{\epsilon^2 (\mu/Pr) (1 + \bar{n} n_{sh} \kappa)} - \frac{n_{sh} \rho v}{\epsilon^2 (\mu/Pr)} \quad (3a)$$

$$\alpha_2 = 0 \quad (3b)$$

$$\alpha_3 = \frac{n_{sh}}{(\mu/Pr)} \frac{\partial \phi}{\partial \eta} \frac{\partial g}{\partial \bar{n}} + \frac{n_{sh}^2}{(\mu/Pr)} \left[\frac{\kappa}{(1 + \bar{n} n_{sh} \kappa)} + \frac{j \cos \theta}{r + \bar{n} n_{sh} \cos \theta} \right] \phi + \frac{n_{sh} v}{\epsilon^2 (\mu/Pr)} \frac{\partial p}{\partial \eta} \frac{\partial g}{\partial \bar{n}} \quad (3c)$$

$$\alpha_4 = - \frac{n_{sh}^2 \rho u}{\epsilon^2 (\mu/Pr) (1 + \bar{n} n_{sh} \kappa)} \quad (3d)$$

where

$$\phi = \frac{\mu}{Pr} (Pr - 1) \frac{u}{n_{sh}} \frac{\partial u}{\partial \eta} \frac{\partial g}{\partial \bar{\eta}} - \frac{\mu u^2 \kappa}{1 + \bar{\eta} n_{sh} \kappa} \quad (3e)$$

The remaining first-order equations are written as follows:

Global Continuity:

$$\begin{aligned} \frac{\partial}{\partial \xi} [n_{sh} (r + \bar{\eta} n_{sh} \cos \theta)^j \rho u] + \frac{\partial g}{\partial \bar{\eta}} \frac{\partial}{\partial \eta} \{ (r + \bar{\eta} n_{sh} \cos \theta) \\ \times [(1 + \bar{\eta} n_{sh} \kappa) \rho v - n'_{sh} \bar{\eta} \rho u] \} = 0 \end{aligned} \quad (4)$$

n-momentum:

$$\begin{aligned} \frac{\rho u}{(1 + \bar{\eta} n_{sh} \kappa)} \frac{\partial v}{\partial \xi} - \frac{n'_{sh} \bar{\eta} \rho u}{n_{sh} (1 + \bar{\eta} n_{sh} \kappa)} \frac{\partial v}{\partial \eta} \frac{\partial g}{\partial \bar{\eta}} + \frac{\rho v}{n_{sh}} \frac{\partial v}{\partial \eta} \frac{\partial g}{\partial \bar{\eta}} \\ - \frac{\rho u^2 \kappa}{(1 + \bar{\eta} n_{sh} \kappa)} + \frac{1}{n_{sh}} \frac{\partial p}{\partial \eta} \frac{\partial g}{\partial \bar{\eta}} = 0 \end{aligned} \quad (5)$$

state:

$$p = \rho T(\gamma - 1) / \gamma. \quad (6)$$

In Eqs. (2) through (5), prime denotes differentiation with respect to ξ . Further, Eqs. (1) through (5) contain the following independent transformation (Ref. 20):

$$\eta = g\left(\frac{n}{n_{sh}}\right) = g(\bar{\eta}). \quad (7a)$$

The stretching function $g(\bar{\eta})$ is given by

$$g(\bar{\eta}) = 1 - \left[\bar{\alpha} + \frac{(1-\bar{\alpha})}{\ln\left(\frac{\bar{\beta}+1}{\bar{\beta}-1}\right)} \ln \left\{ \frac{\bar{\beta} - \bar{\eta}(2\bar{\alpha}+1) + 1}{\bar{\beta} + \bar{\eta}(2\bar{\alpha}+1) - 1} \right\} \right] \quad (7b)$$

and its first and second derivatives are

$$\frac{dg}{d\bar{\eta}} = \frac{(1-\bar{\alpha})(2\bar{\alpha}+1)}{\ln\left(\frac{\bar{\beta}+1}{\bar{\beta}-1}\right)} \left\{ \frac{1}{[\bar{\beta} - \bar{\eta}(2\bar{\alpha}+1) + 1]} + \frac{1}{[\bar{\beta} + \bar{\eta}(2\bar{\alpha}+1) - 1]} \right\} \quad (7c)$$

$$\frac{d^2g}{d\bar{\eta}^2} = \frac{(1-\bar{\alpha})(2\bar{\alpha}+1)^2}{\ln\left(\frac{\bar{\beta}+1}{\bar{\beta}-1}\right)} \left\{ \frac{1}{[\bar{\beta} - \bar{\eta}(2\bar{\alpha}+1) + 1]^2} - \frac{1}{[\bar{\beta} + \bar{\eta}(2\bar{\alpha}+1) - 1]^2} \right\} \quad (7d)$$

Equation (7b) permits the mesh to be refined either near the body ($\bar{\alpha} = 0$) or refined equally near both the body and bow shock ($\bar{\alpha} = 1/2$) when shock becomes thick under the low density flight conditions. Parameter $\bar{\beta}$ controls the amount of refinement with values near 1 giving the largest amount of stretching. Equation (7b) may be inverted to obtain the physical coordinate $\bar{\eta}$ from the transformed coordinate η :

$$\bar{\eta} = \frac{1}{(2\bar{\alpha}+1)} \left[1 - \bar{\beta} \frac{\left\{ \frac{\frac{1-\eta-\bar{\alpha}}{\left(\frac{\bar{\beta}+1}{\bar{\beta}-1}\right)^{1-\bar{\alpha}}} - 1}{\frac{\frac{1-\eta-\bar{\alpha}}{\left(\frac{\bar{\beta}+1}{\bar{\beta}-1}\right)^{1-\bar{\alpha}}} + 1} \right\}}{1} \right] \quad (7e)$$

The transformation of Eq. (7a) keeps the body at $\eta = 0$ and the shock at $\eta = 1$ with uniform mesh in the computational coordinate η .

For ease in numerical computations, Eqs. (1) through (6) are further transformed by normalizing most of the variables with their local shock values. The normal velocity v is not normalized because this quantity changes direction at the shock and can be near zero. Therefore, the normalized v -profiles may not be well behaved.

Boundary Conditions

The following wall and shock-boundary conditions are employed.

Surface Conditions (Ref. 21)

(i) Velocity Slip

$$u_s = \sqrt{\frac{\pi}{2}} \left(\frac{2 - \bar{\theta}}{\bar{\theta}} \right) \frac{\epsilon^2 \mu_s}{\sqrt{p_s \rho_s}} \left[\frac{1}{n_{sh}} \frac{\partial g}{\partial \bar{\eta}} \frac{\partial u}{\partial \bar{\eta}} - \frac{\kappa u}{(1 + \bar{\eta} n_{sh} \kappa)} \right]_s \quad (8a)$$

(ii) Pressure Slip

$$p_s = p_w + \frac{4}{5 \sqrt{2\pi}} \left(\frac{\gamma}{\gamma-1} \right) \left(\frac{2-\bar{\theta}}{\bar{\theta}} \right) \frac{\epsilon^2 \mu_s}{Pr T_s} \sqrt{\frac{p_s}{\rho_s}} \left(\frac{1}{n_{sh}} \frac{\partial g}{\partial \bar{\eta}} \frac{\partial T}{\partial \bar{\eta}} \right)_s \quad (8b)$$

(iii) Temperature Slip

$$T_s = T_w + \frac{1}{2} \sqrt{\frac{\pi}{2}} \left(\frac{\gamma}{\gamma-1} \right) \left(\frac{2-\bar{\theta}}{\bar{\theta}} \right) \frac{\epsilon^2 \mu_s}{Pr \sqrt{p_s \rho_s}} \left(\frac{1}{n_{sh}} \frac{\partial g}{\partial \bar{\eta}} \frac{\partial T}{\partial \bar{\eta}} \right)_s \quad (8c)$$

Shock Conditions (Ref. 19)

(1) Continuity

$$\rho_{sh} \tilde{v}_{sh} = - \sin \alpha \quad (9a)$$

(ii) s-momentum

$$\epsilon^2 \mu_{sh} \left\{ \left[\cos(\alpha-\theta) + \bar{n} \frac{\partial n_{sh}}{\partial \xi} \sin(\alpha-\theta) \right] \frac{1}{n} \frac{\partial g}{\partial \bar{n}} \frac{\partial \tilde{u}}{\partial \eta} - \frac{\partial \tilde{u}}{\partial \xi} \sin(\alpha-\theta) \right\}_{sh} + \tilde{u}_{sh} \sin \alpha = \sin \alpha \cos \alpha \quad (9b)$$

(iii) n-momentum

$$p_{sh} = p_{\infty} + \sin \alpha (\sin \alpha + \tilde{v}_{sh}) \quad (9c)$$

(iv) Energy

$$\epsilon^2 \left(\frac{\mu}{Pr} \right)_{sh} \left\{ \left[\cos(\alpha-\theta) + \bar{n} \frac{\partial n_{sh}}{\partial \xi} \sin(\alpha-\theta) \right] \frac{1}{n} \frac{\partial g}{\partial \bar{n}} \frac{\partial T}{\partial \eta} - \frac{\partial T}{\partial \xi} \sin(\alpha-\theta) \right\}_{sh} + T_{sh} \sin \alpha - \frac{\sin \alpha}{2} (\tilde{u}_{sh} - \cos \alpha)^2 \\ = \frac{\sin \alpha}{2} \left\{ \frac{4\gamma}{(\gamma+1)^2} \sin^2 \alpha + \left[\left(\frac{2}{\gamma-1} \right) - \frac{4(\gamma-1)}{(\gamma+1)^2} \right] \frac{1}{M_{\infty}^2} - \frac{4}{(\gamma+1)^2 M_{\infty}^4 \sin^2 \alpha} \right\} \quad (9d)$$

(v) Equation of State

$$\rho_{sh} = \gamma p_{sh} / (\gamma-1) T_{sh}. \quad (9e)$$

In Eqs. (9a) through (9e), \tilde{u} and \tilde{v} are the components of velocity tangent and normal to the shock interface, respectively, and are related to the

components in the body-oriented coordinates as:

$$\tilde{u}_{sh} = u_{sh} \cos(\alpha-\theta) + v_{sh} \sin(\alpha-\theta) \quad (9f)$$

$$\tilde{v}_{sh} = -u_{sh} \sin(\alpha-\theta) + v_{sh} \cos(\alpha-\theta). \quad (9g)$$

There are errors in the expressions for surface pressure and temperature slip (i.e., Eqs. (2.7c) and (2.7d)) of Ref. 19. The pressure and temperature slip values are underpredicted there by the ratio of K/μ as explained in Ref. 21. For a perfect gas this ratio is the same as $1/Pr$. Similarly, Eqs. (2.8d) and (2.8e) of Ref. 19 for the tangential velocity and temperature slip at the shock contain normal derivatives of the shock quantities in the body-oriented coordinate system in place of the shock-oriented coordinates as given by the underlined terms in Eqs. (9b) and (9d).

METHOD OF SOLUTION

The method of solution employed here is an implicit finite-difference method of Refs. 11 and 19. However, this method is implemented here differently from Refs. 11 and 19 because convergence problems were encountered in these references with the increase in shock-layer thickness.

Let the subscript m denote the station measured along the body surface and n denote the station measured normal to the body surface. The second-order equations (1) through (3) are replaced with central differences taken in the η direction and two-point backward differences in the ξ direction at the point (m,n) . Further, based on the hypersonic small disturbance theory for a slender body, the first-order global continuity Eq. (4) and n -momentum

Eq. (5) are solved for the pressure, p , and normal velocity, v , in a coupled way. The density in these equations is eliminated through the use of equation of state, Eq. (6). Each of the Eqs. (4) and (5) are expressed in finite-difference form at points $(m, n + 1/2)$ and $(m, n - 1/2)$ using a box scheme discussed by Richtmyer (Ref. 32). In these two coupled equations, p and v are eliminated alternatively to solve for these two variables. The finite-difference forms of Eqs. (1) through (5) can easily be solved by using the Thomas Algorithm.

The solution is started at the stagnation point where the various flowfield quantities are expanded (Refs. 11 and 20) in terms of the distance, ξ , along the body surface. These series expansions reduce the partial differential equations (1) through (5) to ordinary differential equations in terms of η . At a body location m , other than the stagnation point, a two-point backward difference is used for the derivative with respect to ξ at the point (m, n) as mentioned earlier. This again gives ordinary differential equations at location m in terms of η for equations (1) through (5). The finite-difference form of these ordinary differential equations (obtained through the central differences) can be solved by using the Thomas Algorithm as mentioned earlier. Figures 2a, 2b, and 2c present the flow diagrams for obtaining solutions with body slip, shock-slip, and body and shock-slip, respectively.

DISCUSSION OF RESULTS

Some of the obtained results by the present method are given in Figures 3 through 13.

Reference 19 carried out some of the early detailed calculations for the low density flow conditions. In Refs. 11 and 19, the governing equations are solved in a successive manner and an initial shock shape is required as an input so as to make the viscous shock-layer equations (which are weakly elliptic in the tangential direction) parabolic. This allows the use of a numerical scheme with space marching in the streamwise direction. In the approach of Refs. 11 and 19, the initial shock shape is obtained from the thin-shock-layer approximation, whereas Refs. 23 and 24 have obtained it from an inviscid solution. Both of these approaches are unworkable under the low-density conditions, especially for a slender body. In the present method of solution, the initial shock shape is obtained from the corresponding cone angle solution (Ref. 26) for a high Reynolds number flow case. For a very low Reynolds number, the initial shock shape may be obtained by reducing the Reynolds number sequentially by a factor of 10 or so. This approach gives very good estimate of the initial shock shape and results in consistent convergence of the solutions. An alternate method, which avoids prescription of the initial shock shape, has recently (Ref. 33) been suggested for the high density flows. However, this method is not suitable for long slender bodies. Moreover, for the faster convergence and stability, a good initial shock shape is desirable for this method also. In the present approach, the continuity and normal momentum equations are solved simultaneously as a coupled set to overcome the stability problems encountered in Refs. 11 and 19 for slender bodies. The tangential momentum and energy equations are still solved in a

successive manner. As mentioned earlier, Refs. 11 and 19 solve all the governing equations successively.

Detailed comparisons of the predictions with the experimental data of Little (Ref. 30) were made in Ref. 19. These data are still considered quite good. Unfortunately, Little's data are limited to the measurements of pressure, drag, and skin friction only. There are no surface heat transfer data provided. Only good data for the surface heat transfer are obtained in Ref. 31. Thus, there is a considerable need to have the surface heat transfer data under the low density flow conditions.

Figures 3 and 4 give comparisons for the Stanton number and skin-friction coefficient, respectively, obtained by the present method and by that of Ref. 19. The calculations are carried out for the stagnation point only for different values of the Reynolds number parameter ϵ , which is a measure of the degree of rarefaction. Larger values of ϵ imply increased slip (or low density) effects. The two predictions have similar trend. However, significant differences are noticeable for larger values of ϵ . The present calculations give better agreement with the experimental data (as will be shown in Figures 5 through 9) and are, therefore, considered accurate. The discrepancies between the present predictions and those of Ref. 19 may be explained by the following: First, the transformation employed (in the present method) to cluster the computational points near the body and shock gives more accurate slip values. Second, there are some errors (see Ref. 21) contained in Ref. 19 in the surface pressure and temperature slip expressions as well as in the equations giving slip values of tangential velocity and temperature at the shock as discussed earlier. The latter error may not affect the values at the stagnation point.

Figures 5 through 8 give comparisons between the predictions and the experimental data of Ref. 30. Clearly, the drag coefficient (with shock and body slip) predicted by the present method is in much better agreement with the experimental data in comparison to the prediction of Ref. 19, over a wide range of the freestream Reynolds numbers, Re_∞ .

The calculations contained in Figures 2 through 8 are for hyperboloid shaped bodies (see Fig. 1). Figure 9 gives comparison of heat transfer distribution for a ten-degree sphere cone. The present predictions with shock and body slip are in good agreement with the data of Ref. 31 except for the stagnation point. The heat transfer rates at the stagnation point were determined to be biased upward (Ref. 34) due to particle impact caused by the arc heater.

Figures 10 and 11 show comparisons of predicted skin-friction coefficient and Stanton number distributions. The comparison between the present values and those of Ref. 33 is quite good. However, the method of Ref. 33 is fully coupled as compared to the coupling between the normal momentum and continuity equations only in the present method. The full coupling requires solving a 5×5 matrix at every point in the flowfield for a perfect gas. The complexity and stability problems (Ref. 33) in a fully coupled solution will increase in analyzing a seven-species high-temperature air flow. Also, the computational times will be considerably large for long slender bodies by this method. Present approach is more appealing for such flow conditions. Figures 10 and 11 also give results with and without slip for a variable grid near the shock and body surface. Clearly, the computational grid-size as well as the slip effects are important in this case.

Finally, Figures 12 through 14 provide a severe test for the present computational method and the surface and shock-slip boundary conditions. The flow analyzed in these figures is a high Mach number ($M_\infty = 20$) flow over a highly-cooled ($T_w = 540^\circ\text{R}$), one-inch nose radius, 10° sphere cone. The surface drag, Stanton number, and surface pressure distributions are predicted for very high to low altitude flight conditions. As the body moves from low-density to high-density flight regime, the slip effects are gradually reduced and become almost negligible at a height of 50,000 ft. However, they persist to a much lower altitude (namely, 50,000 ft.) due to the highly-cooled surface condition for this high Mach number flow case. Also, the slip effects persist in surface drag and pressure through a wider altitude range as compared to the Stanton number or surface heat transfer.

CONCLUSIONS

Results have been obtained for the surface pressure, drag, heat transfer as well as skin-friction coefficients for hyperboloids and sphere-cone shaped slender and wide-angled bodies under varying degrees of low-density flow conditions. The flow cases analyzed include highly-cooled surfaces in very high Mach number flows. The present method is found to predict various flowfield quantities quite accurately when compared with the experimental data. A logical extension of this work will be to analyze the multicomponent air flow under the low-density conditions. The present results are limited to the flow of a perfect gas only.

REFERENCES

1. Walberg, G. D.; "Aeroassisted Orbit Transfer-Window Opens on Missions," Astronautics and Aeronautics, Vol. 21, No. 11, Nov. 1983, pp. 36-43.
2. Howe, J. T.; "Introductory Aerothermodynamics of Advanced Transportation Systems," AIAA Paper No. 83-0406, January 1983.
3. Martin, J. A., et al.; "Special Section - Orbit-On-Demand Vehicle," Aerospace America, Feb. 1985, pp. 46-48.
4. Watts, J. D., et al.; "Mach 5 Cruise Aircraft Research," Presented at the 1985 Langley Symposium on Aerodynamics, NASA Langley Research Center, April 23-25, 1985.
5. Gupta, R. N., Moss, J. N., Simmonds, A. L., Shinn, J. L. and Zoby, E. V.; "Space Shuttle Heating Analysis with Variation in Angle of Attack and Catalycity," Journal of Spacecraft and Rockets, Vol. 21, March-April 1984, pp. 217-219.
6. Hays, W. D. and Probstein, R. F.; Hypersonic Flow Theory, Academic Press, New York, 1959.
7. Dorrance, W. H.; Viscous Hypersonic Flow, McGraw-Hill Book Co., New York, 1962.
8. Gupta, R. N. and Rodkiewicz, C. M.; "Unsteady Boundary-Layer Induced Pressures at Hypersonic Speed," Physics of Fluids, Vol. 14, No. 7, pp. 1332-1339, July 1971.
9. Gupta, R. N. and Rodkiewicz, C. M.; "Homogeneous and Heterogeneous Vecteded-Injection Cooling at Hypersonic Velocities," Canadian Society of Mech. Eng. Transaction, Vol. 5, No. 4, pp. 205-214, 1978-79.
10. Gupta, R. N., Joshi, S. P. and Rodkiewicz, C. M.; "Hypersonic Slender-Wedge Analysis with Gradual Change in Angle of Attack," Acta Mechanica, Vol. 47, Springer-Verlag, 1983, pp. 107-115.
11. Moss, J. N.; "Reacting Viscous-Shock-Layer Solutions with Multicomponent Diffusion and Mass Injection," NASA TR R-411, June 1974.
12. Gupta, R. N., Rodkiewicz, C. M., Varghese, N. K., and Jain, A. C.; "Hypersonic Interactions with Surface Mass Transfer - Part I: Steady Flow," AIAA Journal, Vol. 22, April 1984, pp. 449-450.
13. Gupta, R. N., Rodkiewicz, C. M., Varghese, N. K., and Jain, A. C.; "Hypersonic Interactions with Surface Mass Transfer - Part II: Unsteady Flow," AIAA Journal, Vol. 22, April 1984, pp. 451-452.

14. Gupta, R. N.; "Turbulence Modelling of Flowfields with Massive Surface Ablation," J. Spacecraft and Rockets, Vol. 22, November-December, 1983, pp. 531-538.
15. Gupta, R. N.; "Parameters for the Simulation of High Temperature Blown Shock Layers," AIAA J., Vol. 21, February 1983, pp. 314-316.
16. Gupta, R. N., Gnoffo, P. A., and MacCormack, R. W.; "Viscous Shock-Layer Flowfield Analysis by an Explicit-Implicit Method," AIAA J., Vol. 23, No. 5, May 1985, pp. 723-732.
17. Gupta, R. N. and Moss, J. N.; "Effect of Low-Reynolds-Number Turbulence Amplification on Galileo Probe Flowfield," J. Spacecraft and Rockets, Vol. 20, July-August 1983, pp. 409-411.
18. Gupta, R. N., Menon, S., and Rodkiewicz, C. M.; "Analysis of the Strong Interaction Problem with Slip and Temperature-Jump Effects," AIAA J., Vol. 18, No. 7, July 1980, pp. 844-846.
19. Davis, R. T.; "Numerical Solution of the Hypersonic Viscous Shock Layer Equations," AIAA J., Vol. 8, No. 5, May 1970, pp. 843-851.
20. Gupta, R. N. and Simmonds, A. L.; "Hypersonic Low-Density Solutions of the Navier-Stokes Equations with Chemical Nonequilibrium and Multicomponent Surface Slip," AIAA Paper 86-1349, June 1986.
21. Gupta, R. N., Scott, C. D., and Moss, J. N.; "Slip-Boundary Equations for Multicomponent Nonequilibrium Air Flow," NASA TP 2452, November 1985. See also, Progress in Astronautics and Aeronautics, Vol. 96, 1985, pp. 465-490.
22. Tree, I. K., Melson, N. D., and Lewis, C. H.; "Low Reynolds Number Hypersonic Ionizing Viscous Shock-Layer Flows Over the Jovian Probe," AIAA Paper 79-1080, June 1979.
23. Swaminathan, S., Song, D. J., and Lewis, C. H.; "Effects of Slip and Chemical Reaction Models on Three-Dimensional Nonequilibrium Viscous Shock-Layer Flows," J. Spacecraft and Rockets, Vol. 21, November-December 1984, pp. 521-527.
24. Song, D. J. and Swaminathan, S.; "High Altitude Effects on Three-Dimensional Nonequilibrium Viscous Shock-Layer Flows," Vol. 22, November-December 1985, pp. 614-619.
25. Hendricks, W. L.; "Slip Conditions with Wall Catalysis and Radiation for Multicomponent Nonequilibrium Gas Flow," NASA TMX-64942, 1974.
26. Gupta, R. N., Lee, K. P., Moss, J. N., Zoby, E. V., and Tiwari, S. N.; "Hypersonic Viscous Shock-Layer Analysis of Long Slender Bodies - Part I: High Reynolds Number Flow," AIAA Paper 2487, Atmospheric Flight Mechanics Conference, Monterey, CA, August 17-19, 1987.

27. Kim, M. D. Bhutta, B. A., and Lewis, C. H.; "Viscous Shock-Layer Predictions for Hypersonic Laminar or Turbulent Flows in Chemical Equilibrium Over the Windward Surface of a Shuttle-Like Vehicle," AIAA Paper 82-0201, January 1982.
28. Moss, J. N. and Simmonds, A. L.; "Galileo Probe Forebody Flowfield Predictions During Jupiter Entry," AIAA Paper 82-087-4, June 1982.
29. Moss, J. N. and Bird, G. A.; "Direct Simulation of Transitional Flow for Hypersonic Reentry Conditions," AIAA Paper 84-0223.
30. Little, H. R.; "An Experimental Investigation of Surface Conditions on Hyperboloids and Paraboloids at a Mach Number of 10," M.S. Thesis, 1969, University of Tennessee.
31. Boylan, D. E.; "Laminar Heat Transfer on Sharp and Blunt Ten-Degree Cones in Conical and Parallel Low Density Flow," AEDC-TR-73-106, August 1973.
32. Richtmyer, R. D.; Difference Methods for Initial-value Problems, Interscience, New York, 1957.
33. Gordon, R. and Davis, R. T.; "An Improved Method for Solving the Viscous Shock Layer Equations," Tech. Rept., Department of Aerospace Engineering and Engineering Mechanics, University of Cincinnati, September 1985.
34. Boylan, D. E., Private Communication, Severdrup Technology, Inc., Tullahoma, Tennessee, February 1987.

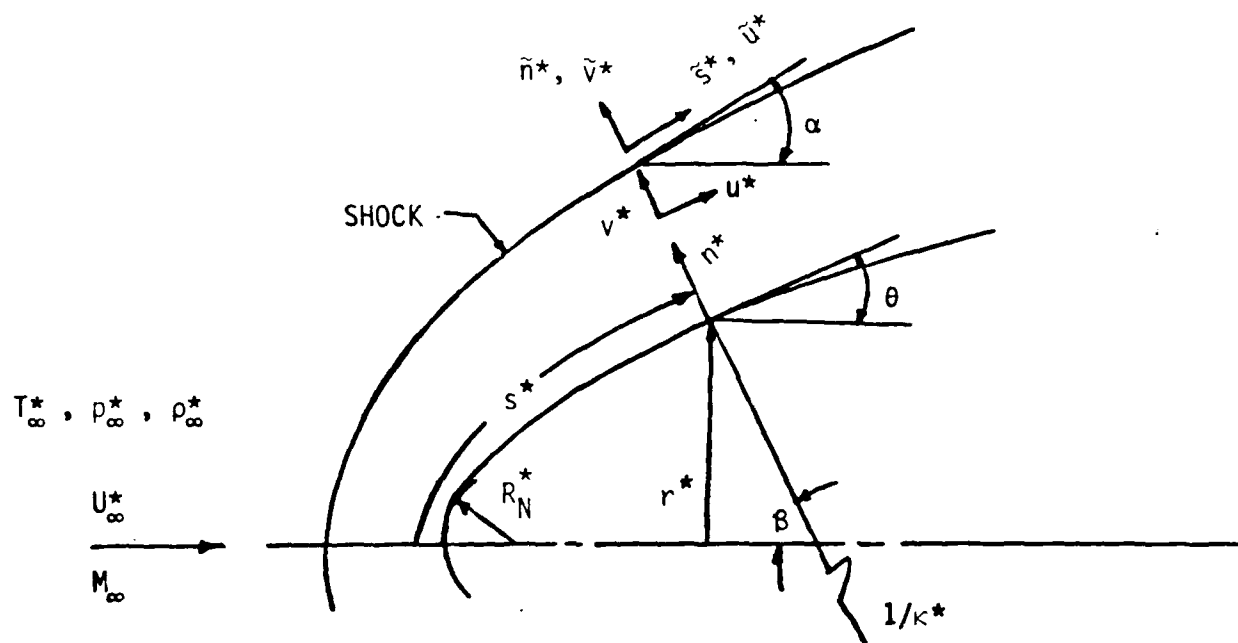


Figure 1. Coordinate System.

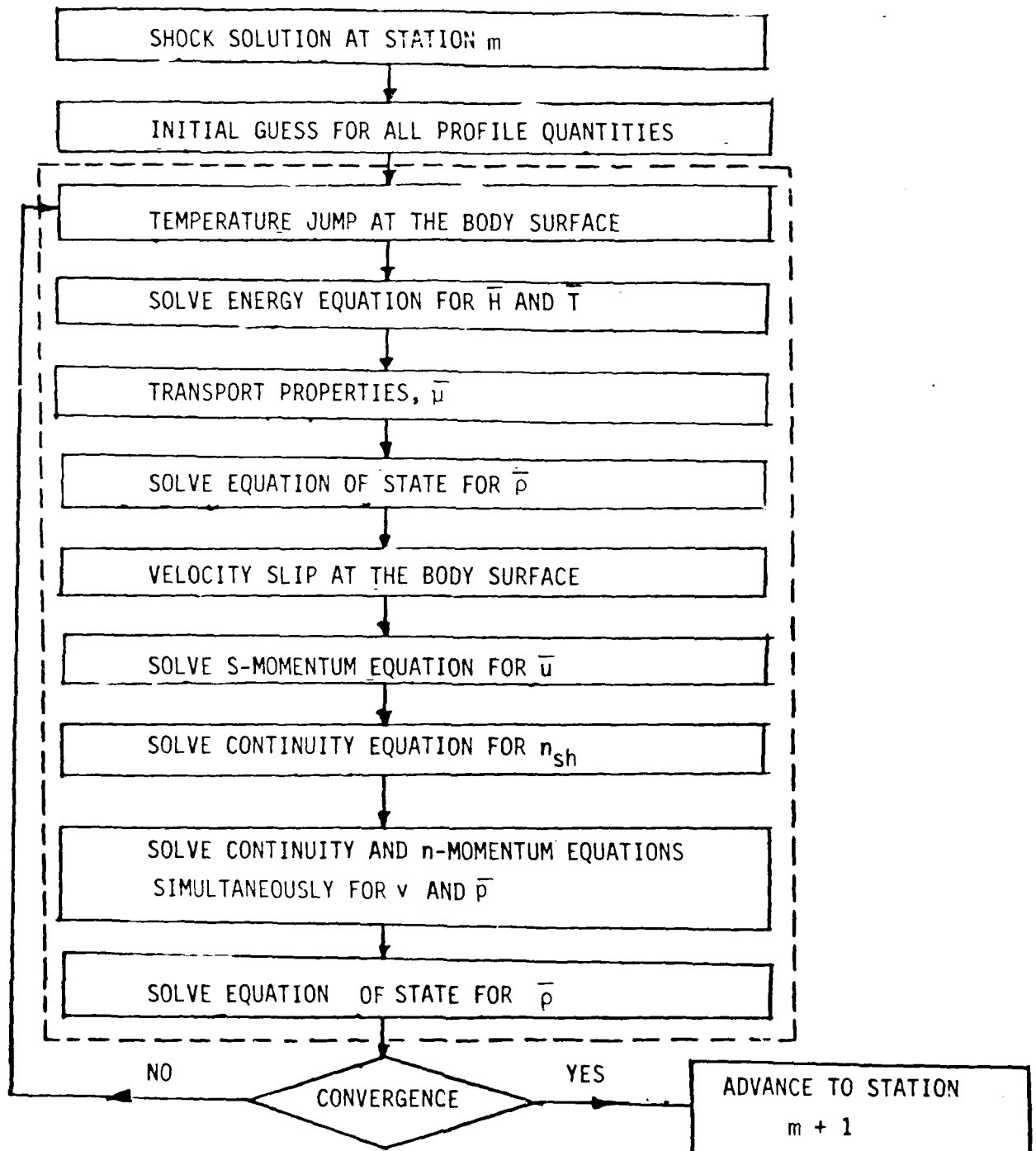


Figure 2a. Flow Chart for Solution Sequence of Viscous-Shock-Layer Equations with Body Slip.

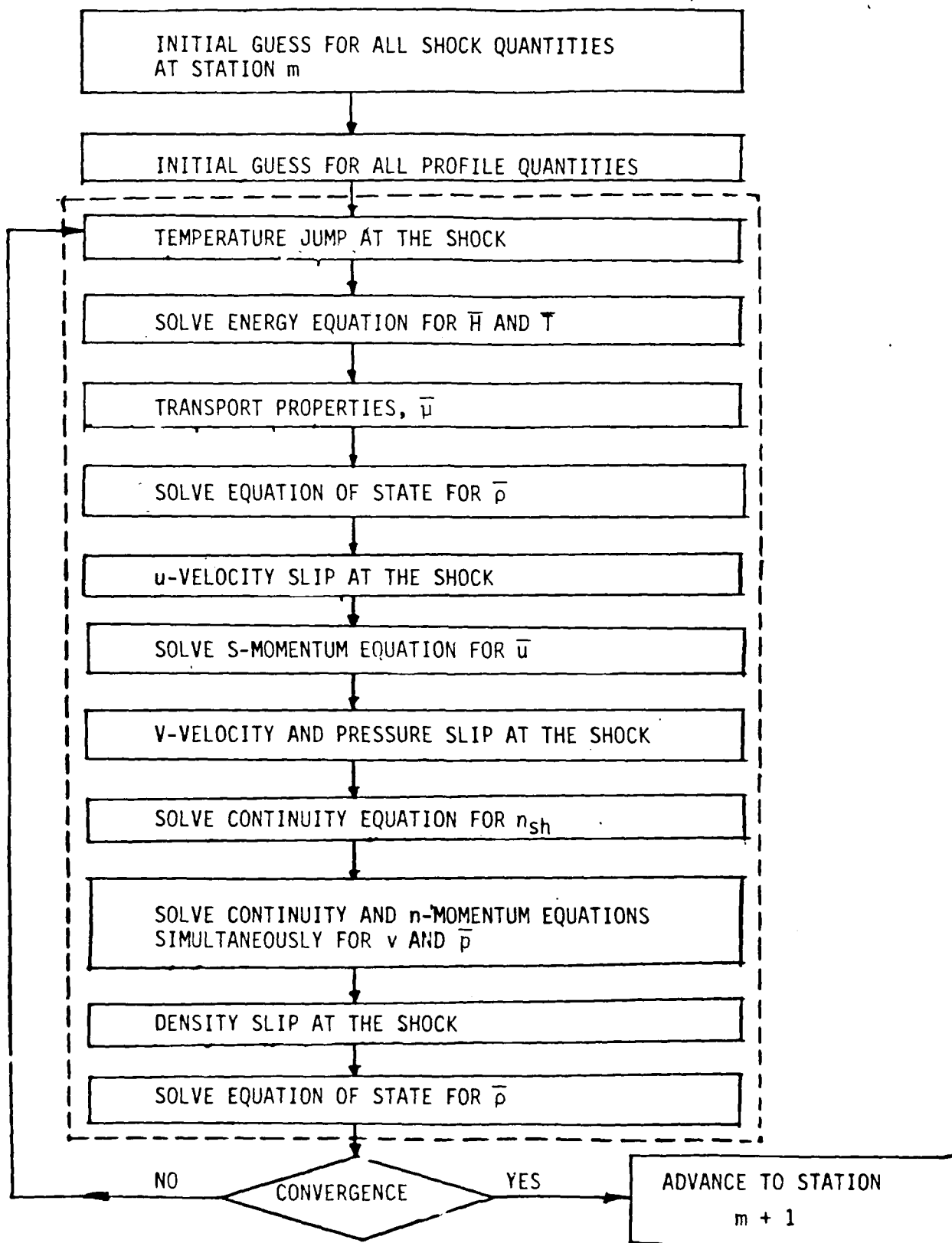


Figure 2b. With Shock Slip.

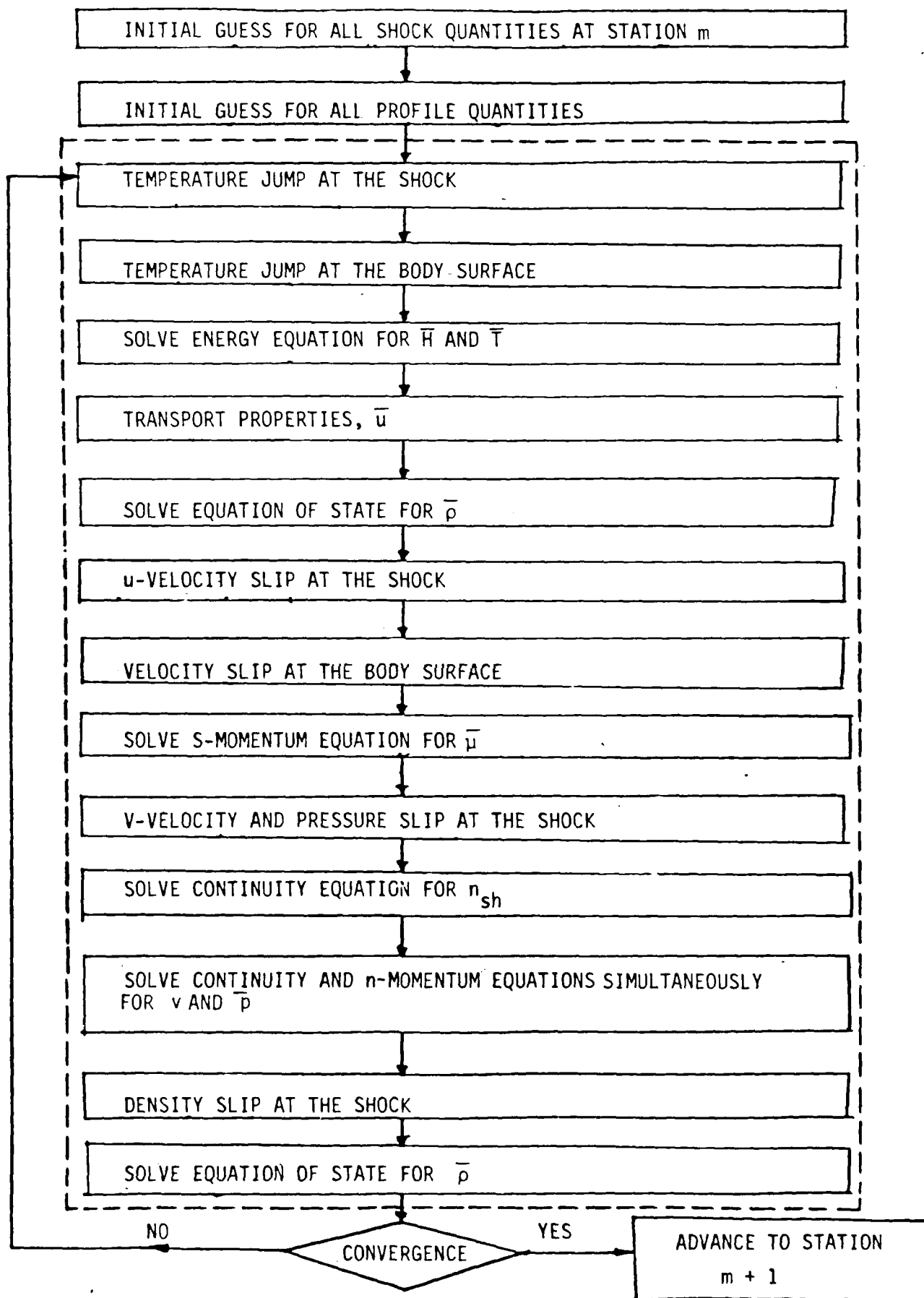


Figure 2c. Shock and Body Slip.

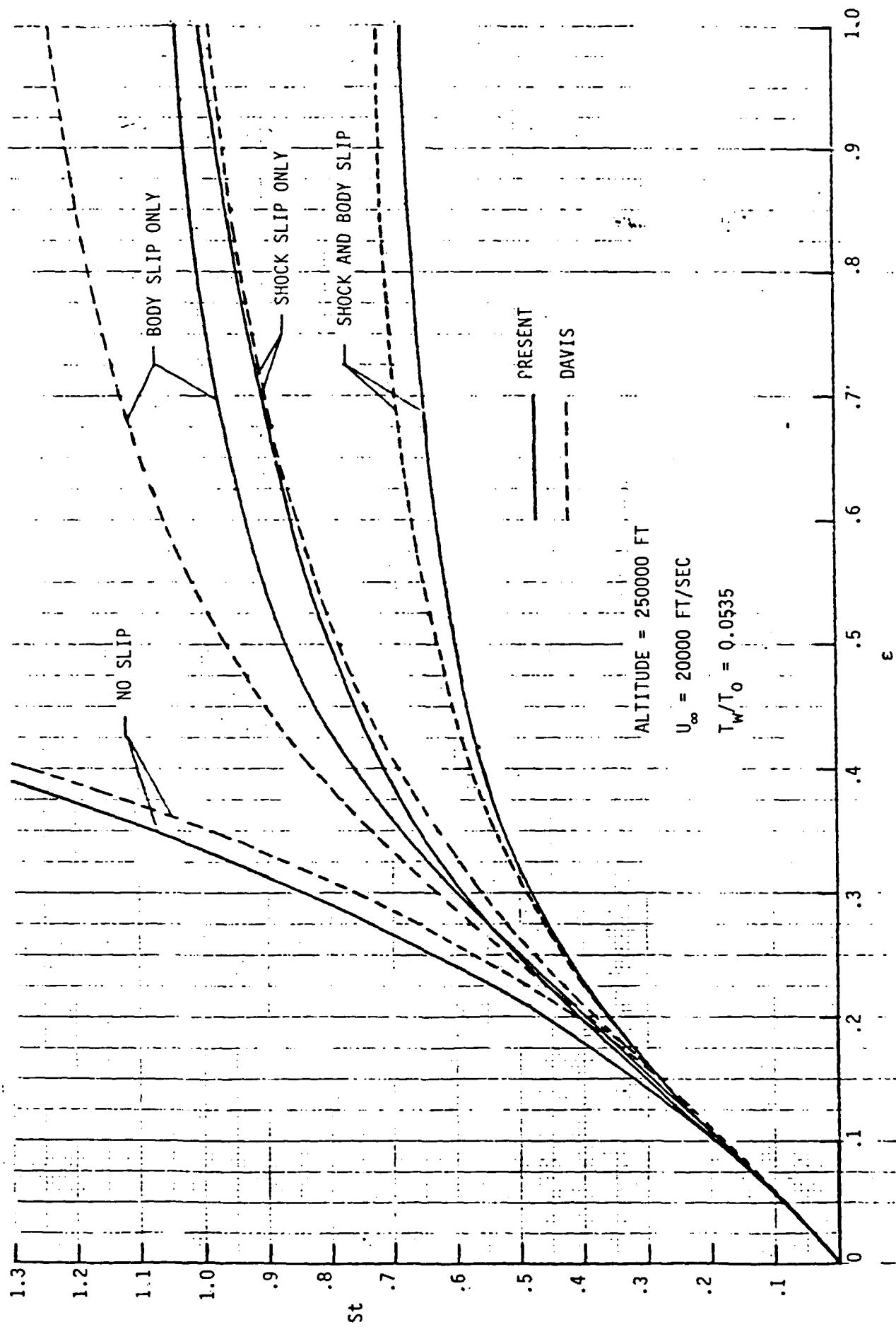


Figure 3. Stanton Number in the Stagnation Point as a Function of ϵ .

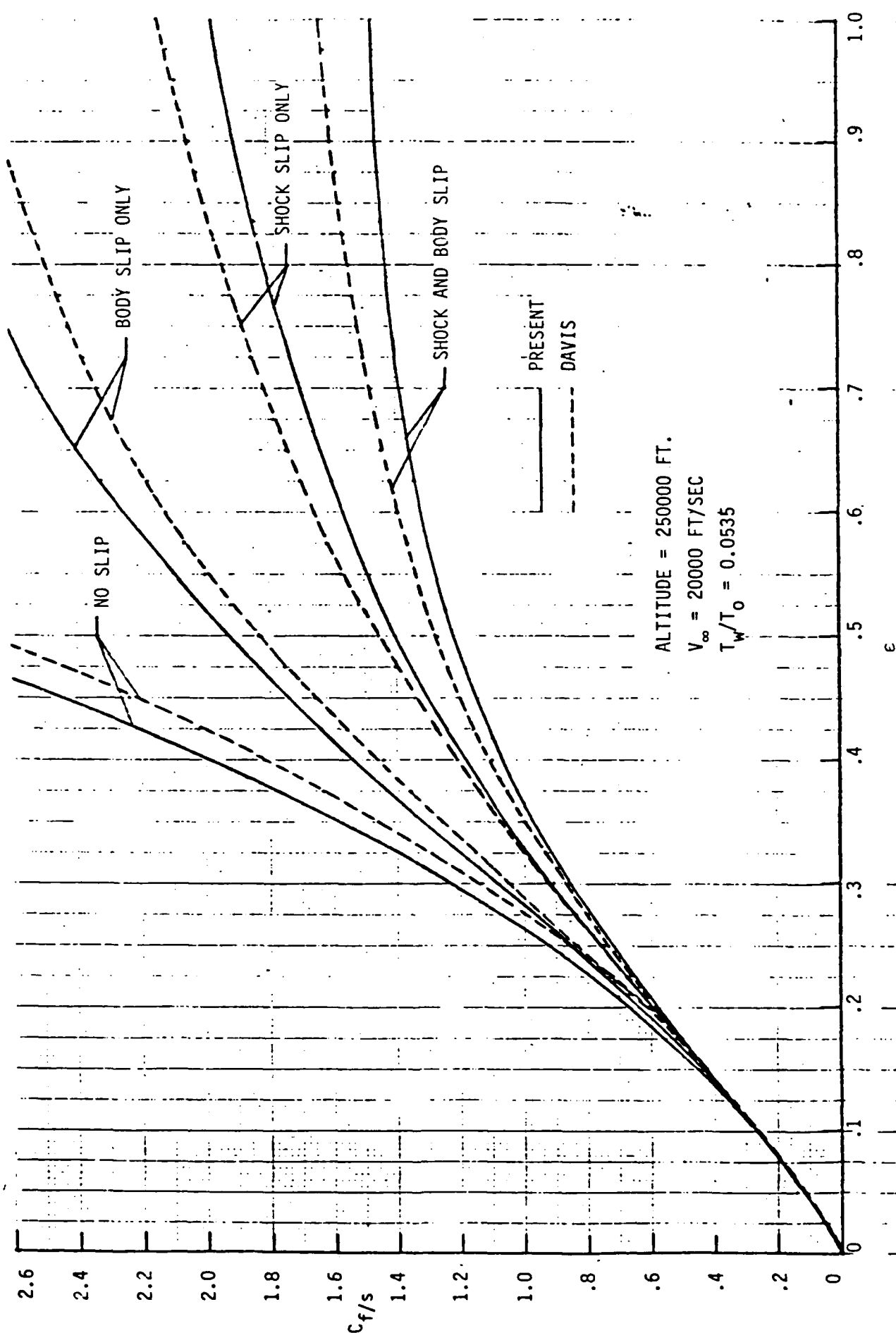


Figure 4. Skin Friction in the Stagnation Point as a Function of ϵ .

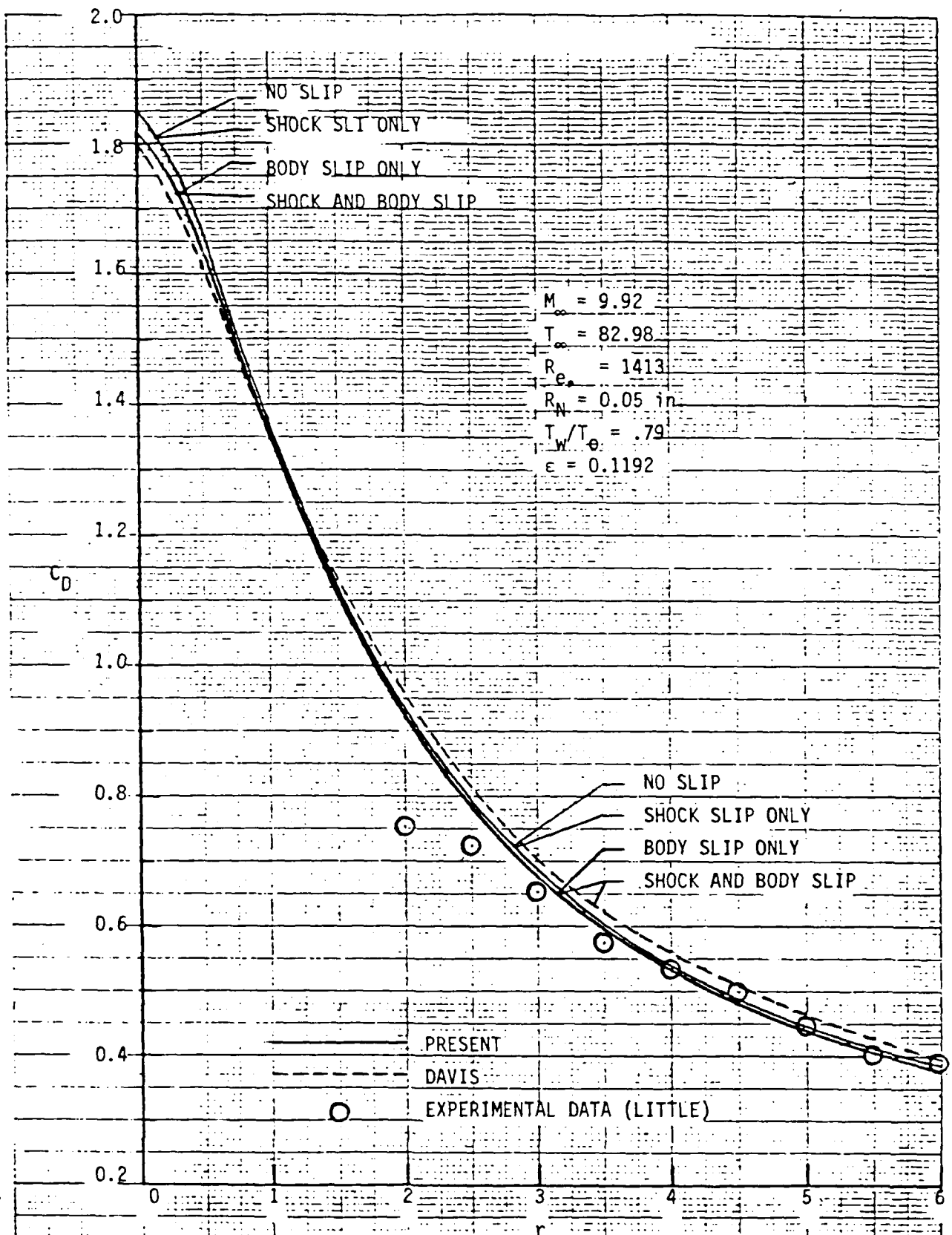


Figure 5. Drag Coefficient for a 10° Hyperboloid.

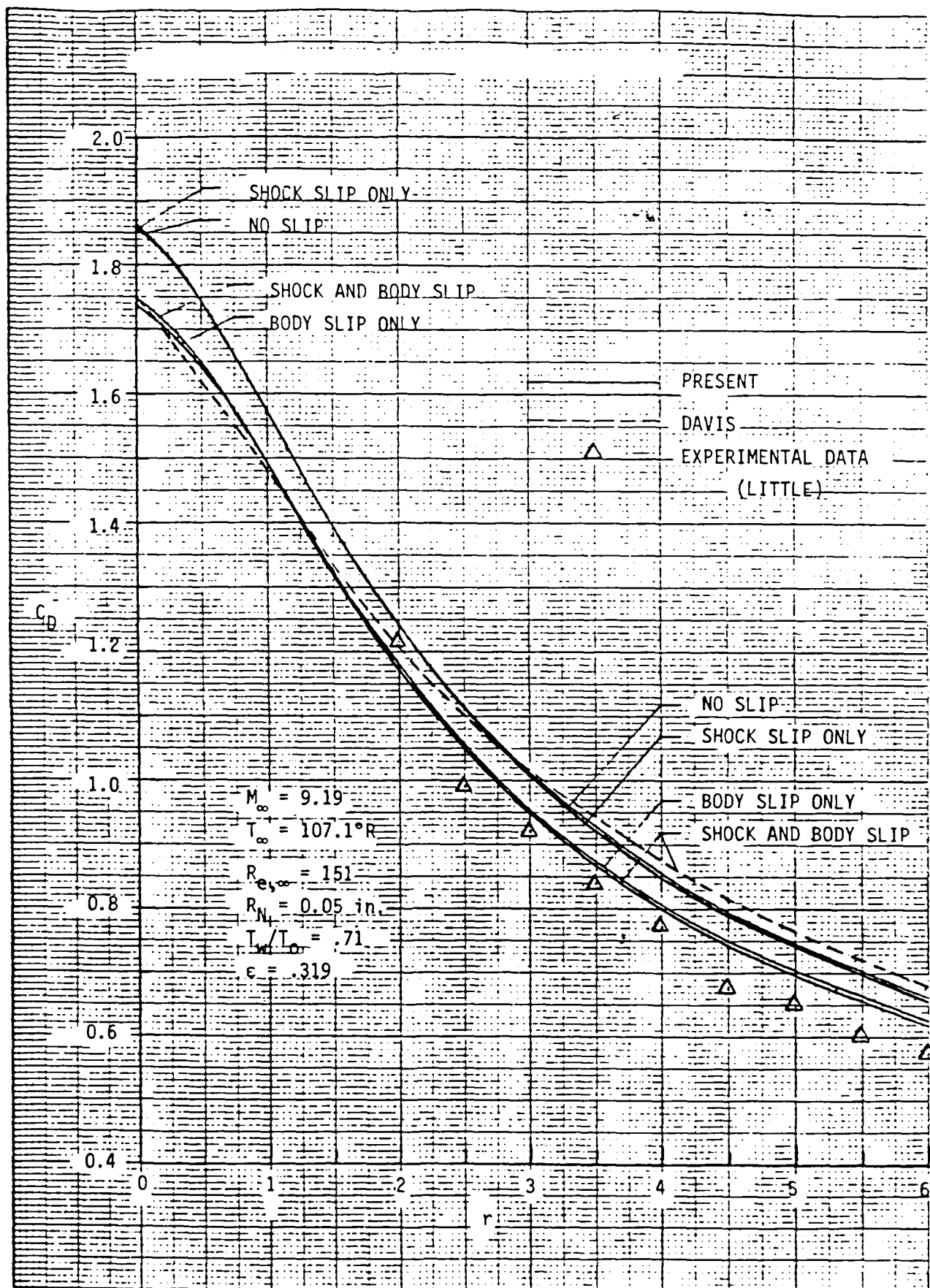


Figure 6. Drag Coefficient for a 10° Hyperboloid.

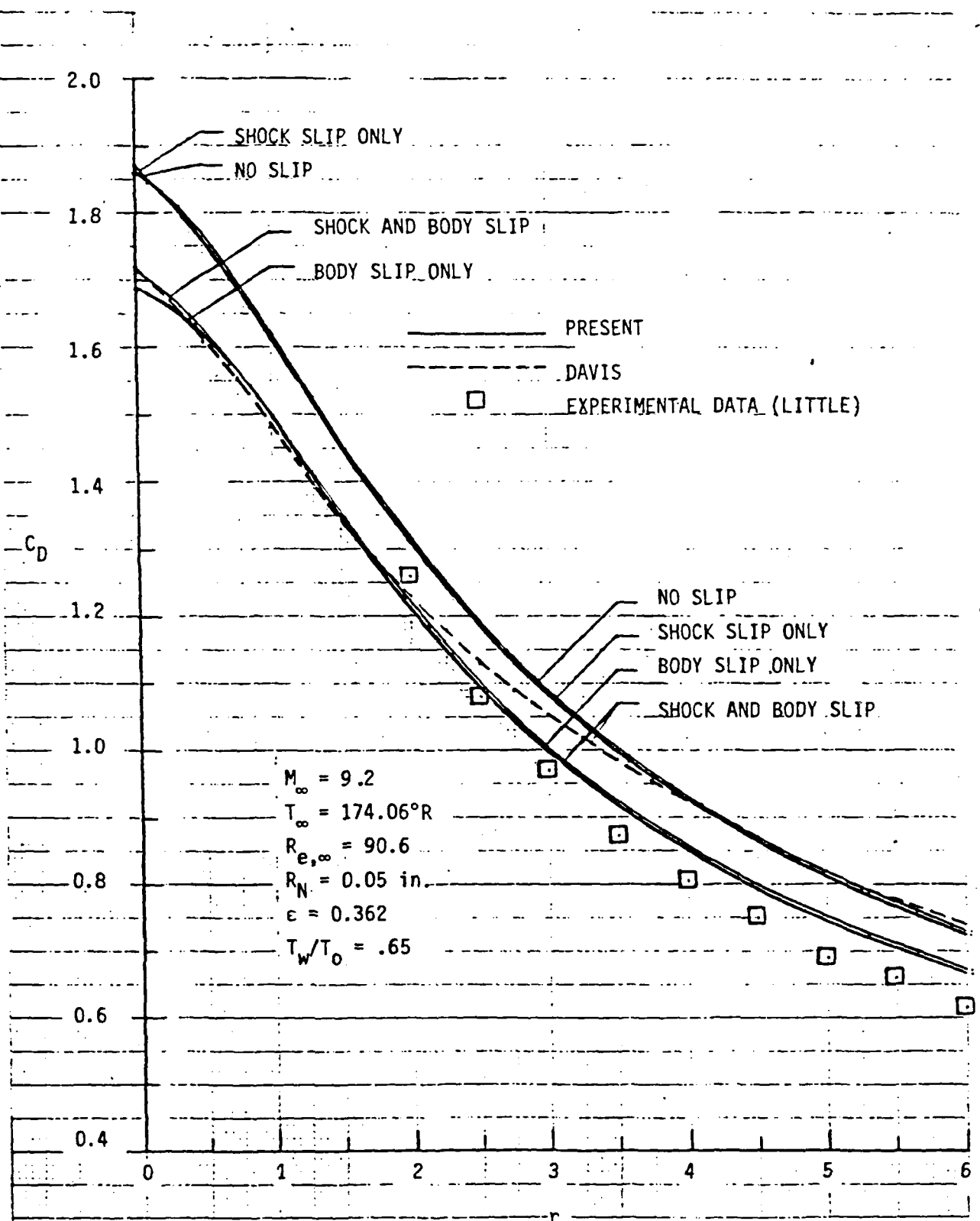


Figure 7. Drag Coefficient for a 10° Hyperboloid.

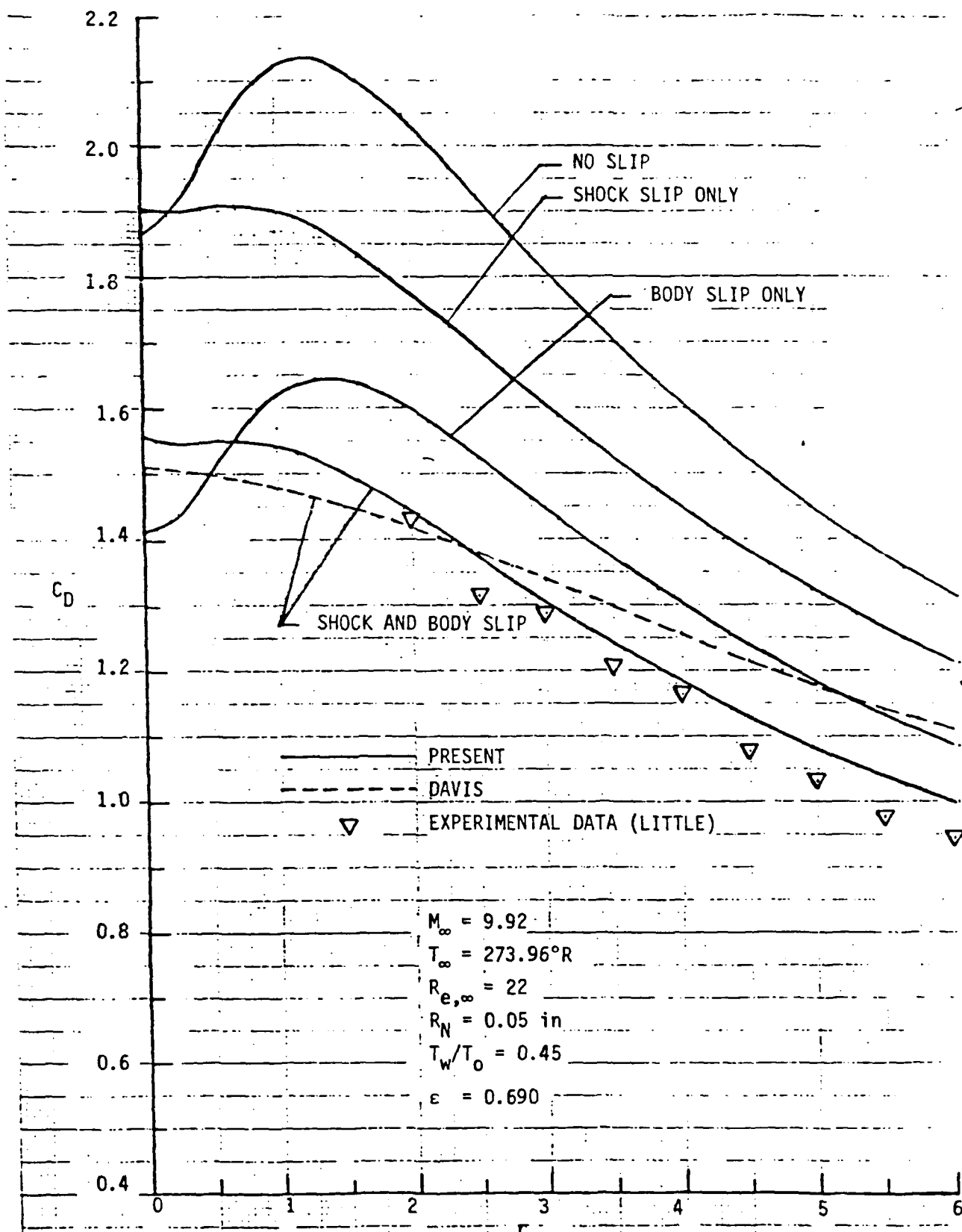


Figure 8. Drag Coefficient for a 10° Hyperboloid.

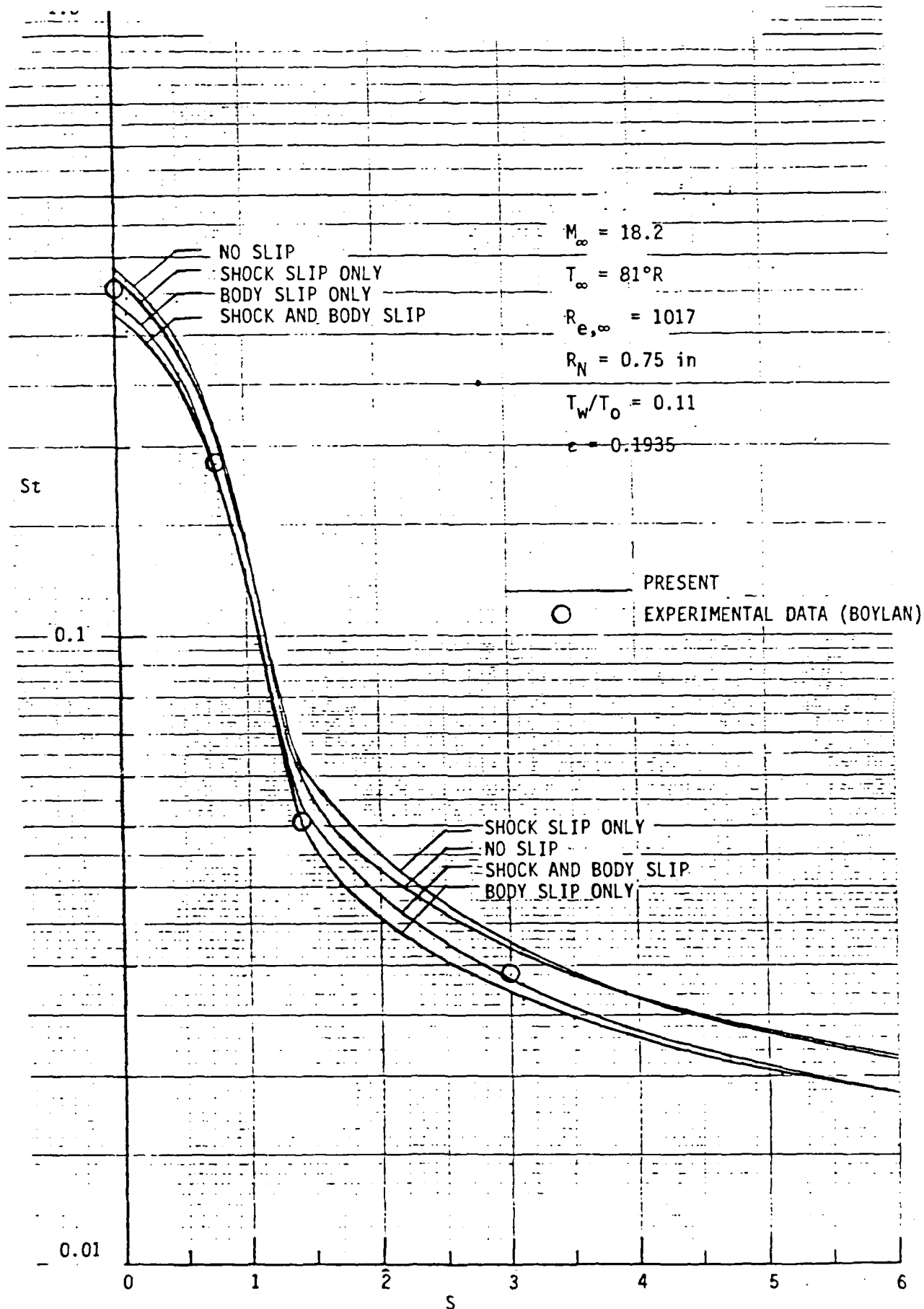


Figure 9. Heat Transfer Distributions Over a 10° Sphere-Cone.

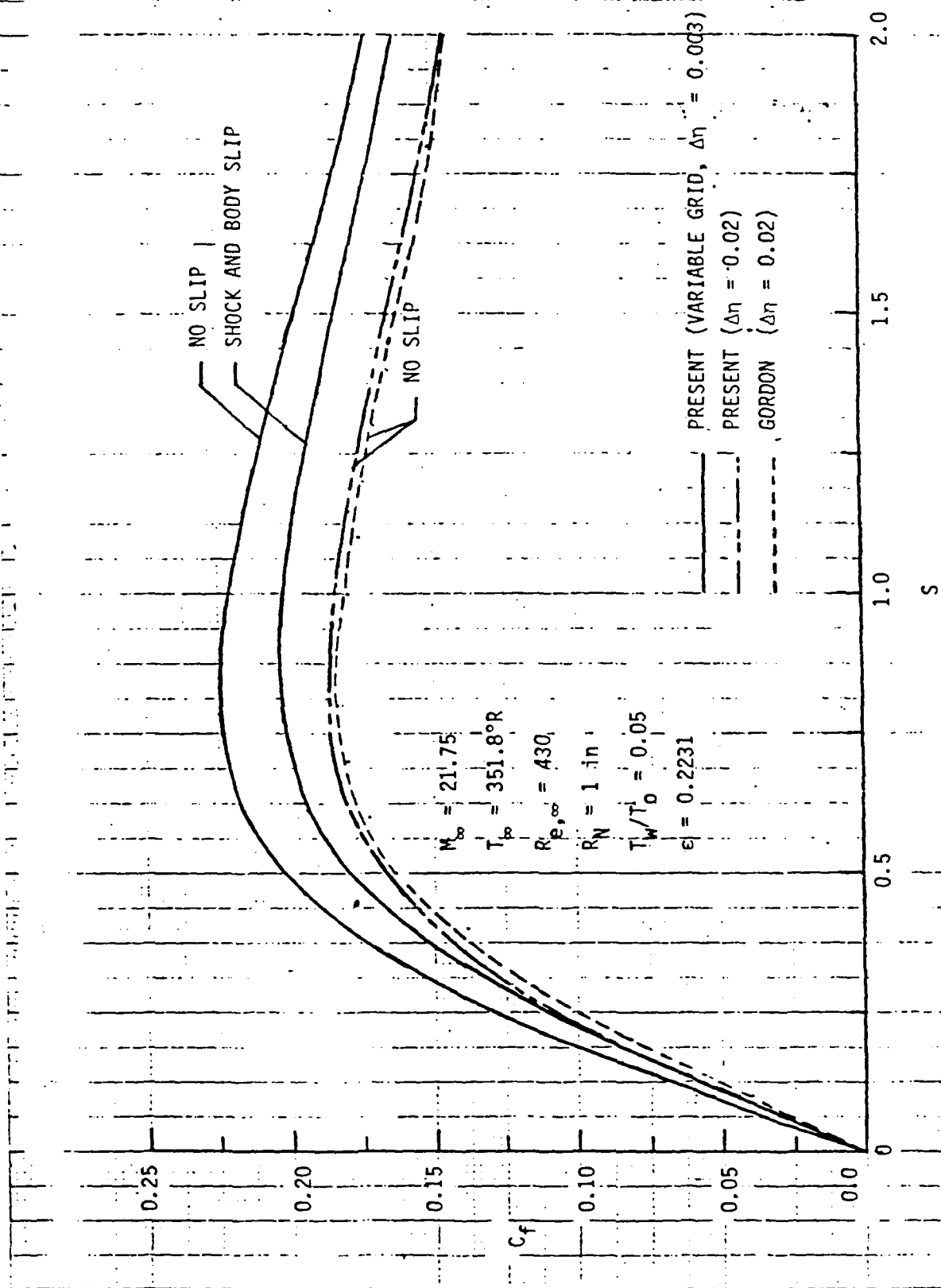


Figure 10. Skin Friction Coefficient Distribution for a 22.5 Hyperboloid.

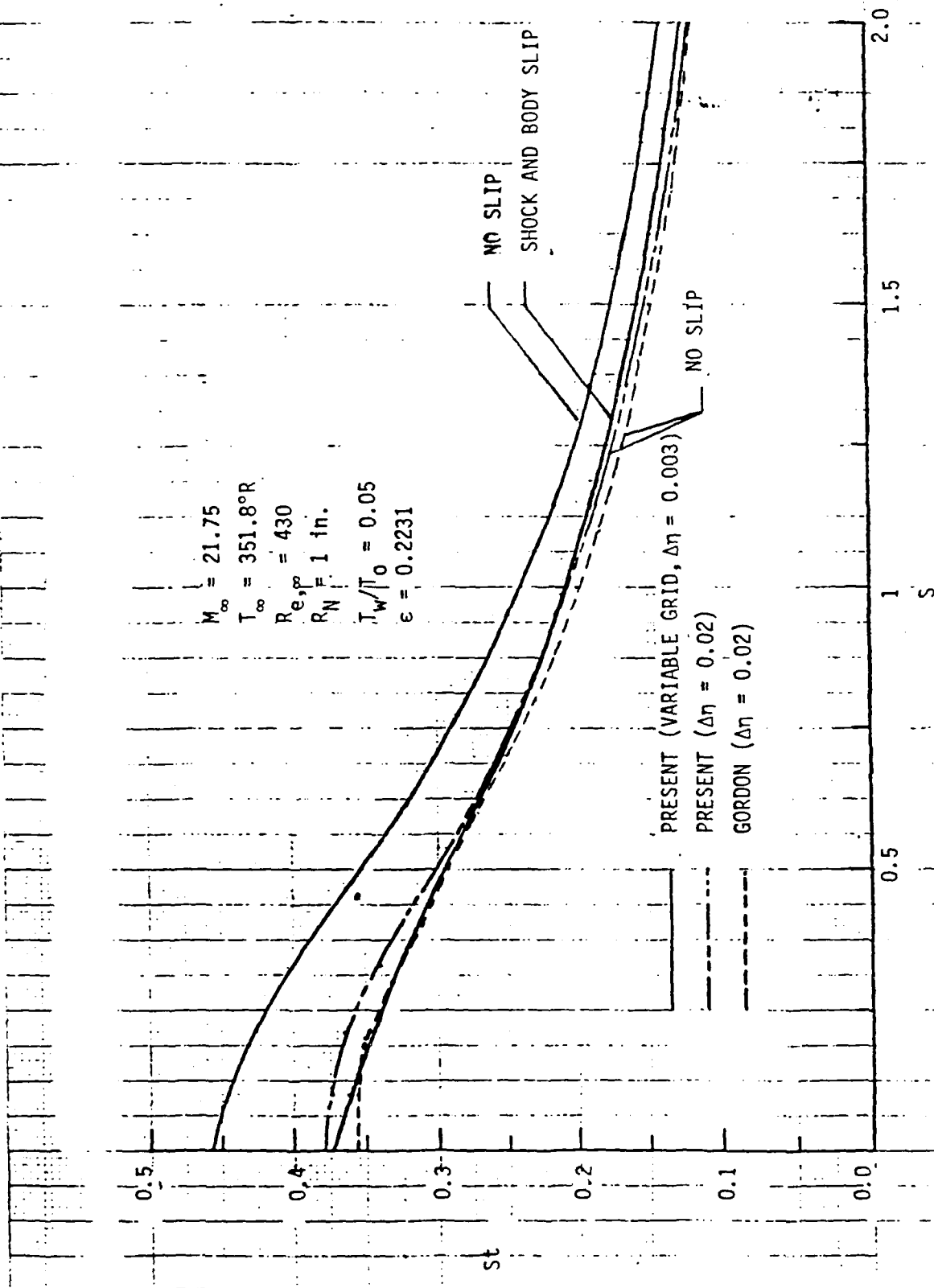


Figure 11. Stanton Number Distribution for a 22.5 Hyperboloid

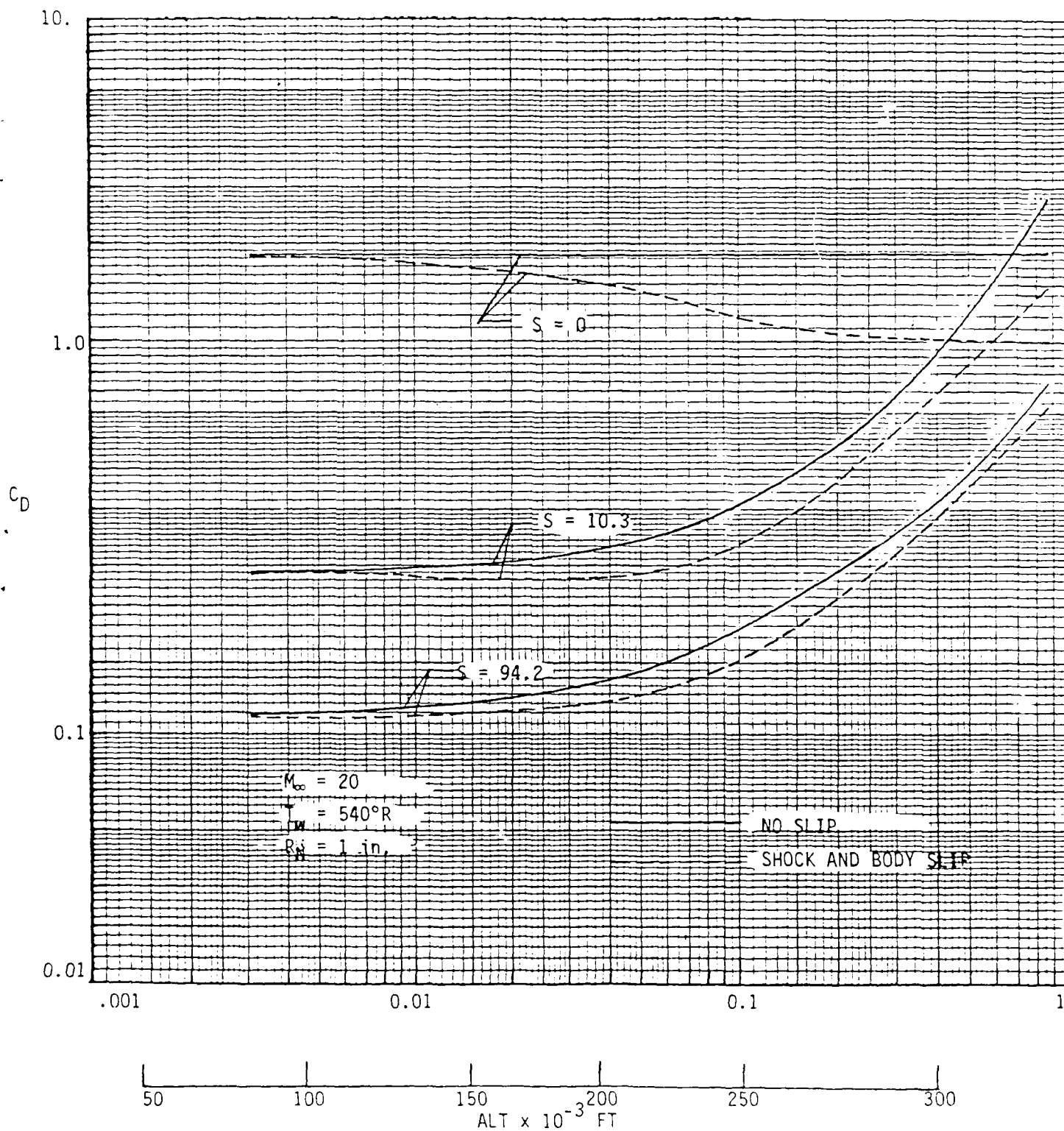


Figure 12. Drag Coefficient as a Function of ϵ for a 10° Sphere-Cone.

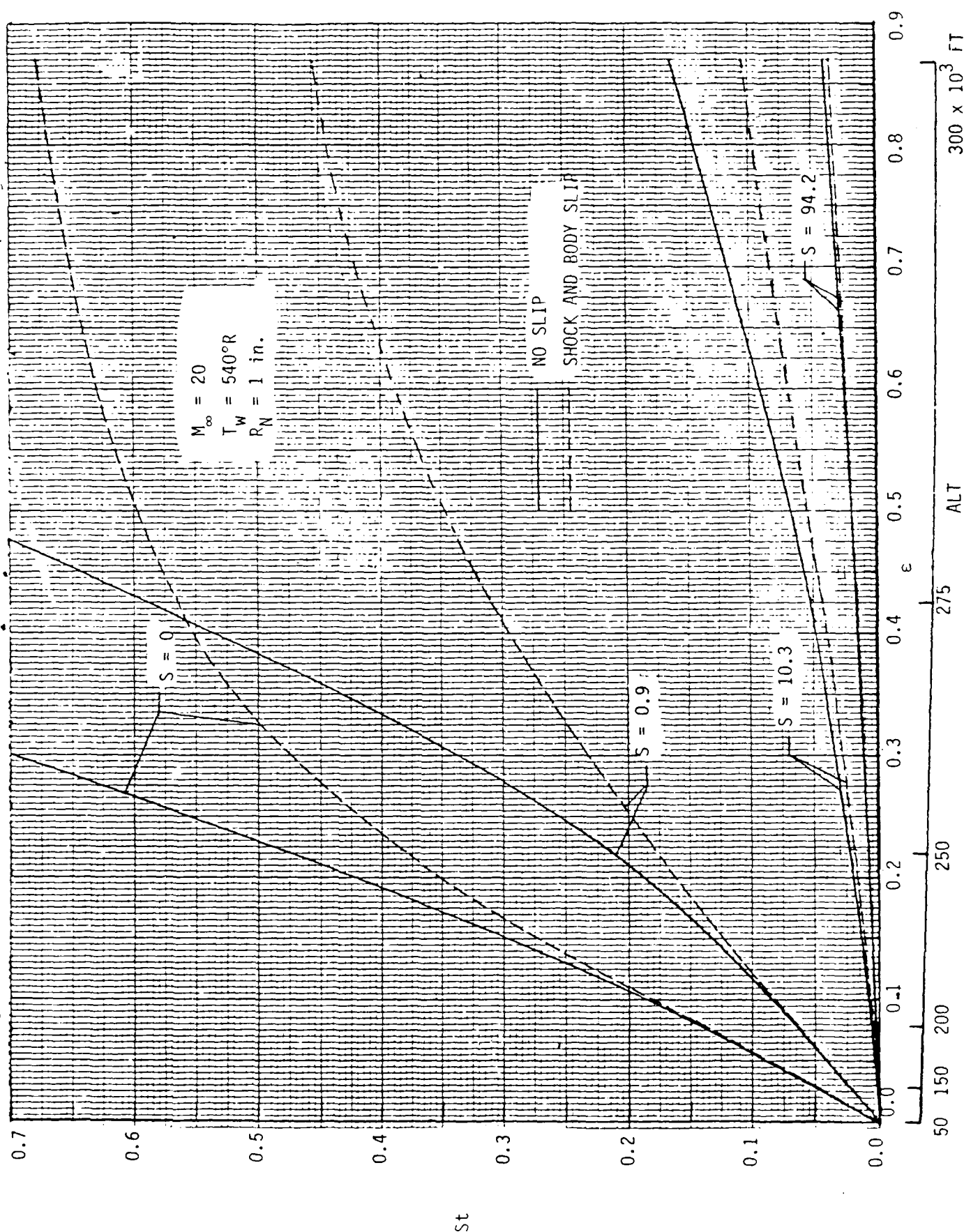


Figure 13. Stanton Number as a Function of ϵ for a 10° Sphere-Cone.

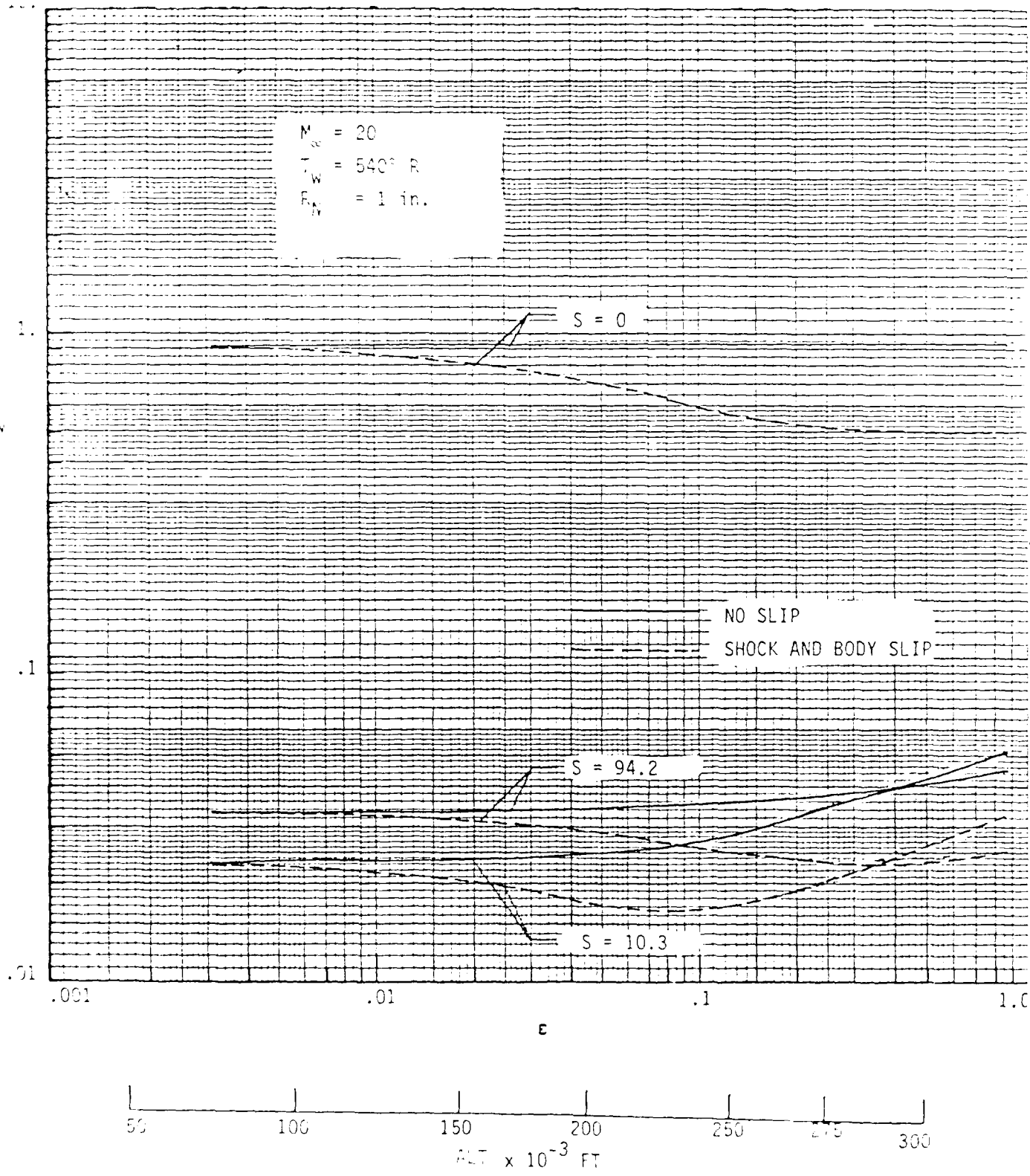


Figure 14. Wall Pressure as a Function of ϵ for a 10° Sphere-Cone.